

UC San Diego

UC San Diego Previously Published Works

Title

Photoacoustic Enhancement of Ferricyanide-Treated Silver Chalcogenide-Coated Gold Nanorods

Permalink

<https://escholarship.org/uc/item/31k6w95t>

Journal

The Journal of Physical Chemistry C, 126(17)

ISSN

1932-7447

Authors

Mantri, Yash
Sit, Izaak
Zhou, Jiajing
[et al.](#)

Publication Date

2022-05-05

DOI

10.1021/acs.jpcc.2c01727

Peer reviewed



Published in final edited form as:

J Phys Chem C Nanomater Interfaces. 2022 May 05; 126(17): 7605–7614. doi:10.1021/acs.jpcc.2c01727.

Photoacoustic Enhancement of Ferricyanide-Treated Silver Chalcogenide-Coated Gold Nanorods

Yash Mantri,

Department of Bioengineering, University of California San Diego, La Jolla, California 92093, United States

Izaak Sit,

Department of Nanoengineering, University of California San Diego, La Jolla, California 92093, United States

Jiajing Zhou,

Department of Nanoengineering, University of California San Diego, La Jolla, California 92093, United States

Vicki H. Grassian,

Department of Chemistry and Biochemistry, University of California San Diego, La Jolla, California 92093, United States

Jesse V. Jokerst

Department of Nanoengineering, Materials Science Program, and Department of Radiology, University of California San Diego, La Jolla, California 92093, United States

Abstract

Plasmonic gold nanorods (AuNRs) are often employed as photoacoustic (PA) contrast agents due to their ease of synthesis, functionalization, and biocompatibility. These materials can produce activatable signals in response to a change in optical absorbance intensity or absorbance wavelength. Here, we report a surprising finding: Ag₂S/Se-coated AuNRs have a ~40-fold PA enhancement upon addition of an oxidant but with no change in absorption spectra. We then study the mechanism underlying this enhancement. Electron micrographs and absorption spectra show good colloidal stability and retention of the core-shell structure after potassium hexacyanoferrate(III) (HCF) addition, ruling out aggregation and morphology-induced PA enhancement. X-ray diffraction data showed no changes, ruling out crystallographic phase changes upon HCF addition, thus leading to induced PA enhancement. Attenuated total reflectance-Fourier transform infrared spectroscopy and zeta potential analysis suggest that PA enhancement is driven by the irreversible displacement of hexadecyltrimethylammonium bromide with HCF.

Corresponding Author: Jesse V. Jokerst – Department of Nanoengineering, Materials Science Program, and Department of Radiology, University of California San Diego, La Jolla, California 92093, United States; jjokerst@ucsd.edu.

Supporting Information

The Supporting Information is available free of charge at <https://pubs.acs.org/doi/10.1021/acs.jpcc.2c01727>.

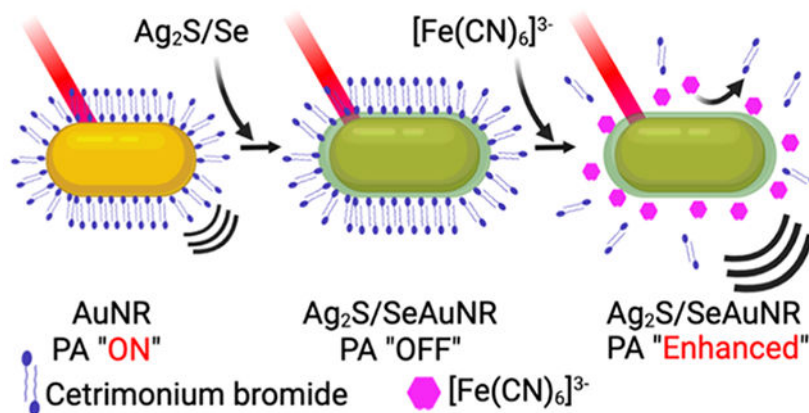
Characterizations of Ag₂Se/AuNRs and AuNRs, experimental setup and data for ATR-FTIR measurements, and additional PA data (PDF)

Complete contact information is available at: <https://pubs.acs.org/10.1021/acs.jpcc.2c01727>

The authors declare no competing financial interest.

This is further confirmed using elemental mapping with energy-dispersive X-ray analysis. PA characterization after HCF addition showed a four-fold increase in the Grüneisen parameter (Γ), thus resulting in PA enhancement. The PA enhancement is not seen in uncoated AuNRs or spherical particles. Two possible mechanisms for PA enhancement are proposed: first, the photo-induced redox heating at the $\text{Ag}_2\text{S}/\text{Se}$ shell–HCF interface, resulting in an increase in temperature-dependent Γ , and second, an enhanced electrostriction response due to HCF adsorption on a layered plasmonic nanoparticle surface, resulting in a high thermal expansion coefficient (β) that is directly proportional to Γ .

Graphical Abstract



INTRODUCTION

Plasmonic gold nanostructures such as spheres and rods are the most widely used nanoparticle-based photoacoustic (PA) contrast agents.^{1,2} Gold nanorods (AuNRs) are particularly useful due to their easily tunable size, high photothermal conversion efficiency, ease of synthesis, functionalization, and a tunable localized surface plasmon resonance (LSPR).^{3–5} We and others have previously reported the use of AuNRs for PA-based cell tracking,⁶ cancer imaging,^{7–9} oxidative stress sensing,¹⁰ and theranostics.^{11,12}

PA imaging uses nanosecond pulsed illumination to generate pressure waves detectable by conventional ultrasound transducers. The absorption of light results in thermally confined heating of the nanoparticle (the millikelvin range).¹³ The increase in temperature causes thermoelastic expansion of the nanoparticle, thus creating pressure transients that propagate through the sample medium.^{1,13} The intensity of the resulting PA signal is a function of the optical and thermo-elastic properties of the nanoparticle and its surroundings (eq 1).^{1,14}

$$\rho_o = \left(\frac{\beta c^2}{C_p} \right) \mu_a F = \Gamma A \quad (1)$$

Here, ρ_o describes the increase in pressure (Pa) measured as a PA signal using conventional ultrasound transducers.¹³ β is the thermal expansion coefficient in K^{-1} ; C_p is the specific heat capacity in $\text{J K}^{-1} \text{kg}^{-1}$; and μ_a is the absorption coefficient in cm^{-1} of the absorbing

material. The term c is the speed of sound in the imaging medium in ms^{-1} ; F is the irradiation fluence in J cm^{-2} . Γ is the Grüneisen parameter ($\beta c^2 C_p^{-1}$) and characterizes the thermo-acoustic conversion efficiency, and A ($\mu_a F$) is the local energy deposition density in J cm^{-3} .^{1,15} An ideal PA contrast agent has a high optical absorption, low scattering properties, and a high photothermal conversion efficiency.^{16–19}

There are various ways to enhance the PA signal generated by AuNRs. The PA intensity is directly proportional to the laser fluence. Increasing the laser fluence and shortening the pulse width can lead to PA enhancement.^{1,20,21} Increasing the nanoparticle concentration results in a higher $\mu\mu_a$ and hence higher PA.^{22–25} AuNR coatings such as silica,^{26–28} polydopamine,^{29,30} titanium dioxide,³¹ and reduced graphene oxide³² have shown significant PA enhancement by reducing the Kapitza resistance (thermal resistance at the particle–solvent interface). This in turn improves thermal confinement to enhance the AuNR PA signal.^{1,20,33} On the contrary, others have shown a reduction of the PA signal on silica coating.³⁴ Studies have also shown that up to 93% of the PA signal is generated by the thermal expansion of the solvent. Hence, using solvents with a high β and low C_p can also enhance the PA intensity.^{14,35,36} Γ of conventional solvents such as water is directly proportional to temperature. Hence, an increase in solvent temperature can also result in PA enhancement.^{14,37} In summary, engineering AuNRs with LSPRs and μ_a responsive to chemical cues is the most common technique for PA signal modulation.^{1,38}

Previously, we investigated the use of silver- and iodide-doped silver-coated AuNRs for oxidative stress sensing.^{10,11} These were shell–core (Ag/AgI–AuNR) that showed selective etching of the shell in the presence of reactive oxygen and nitrogen species (RONS). The bare AuNRs had a near-infrared (NIR) LSPR that blue-shifted upon shell coating, resulting in a low PA signal in the NIR range. Selective etching of the shell layer resulted in full recovery of the AuNR LSPR and its PA signal. In both works, we used potassium hexacyanoferrate(III) (HCF) as a positive control that selectively oxidized the Ag/AgI shell (Ag^+/Ag^0 $E^0 = 0.80$ V). Others have also shown a spontaneous reaction between Ag and $\text{K}_3\text{Fe}(\text{CN})_6$, resulting in the formation of silver HCF(II) and Ag etching off the AuNR core.³⁹ The reduction potential of Au^+/Au^0 ($E^0 = 1.69$ V) is much higher than that of HCF $\text{Fe}^{3+}/\text{Fe}^{2+}$ ($E^0 = 0.77$ V), and hence, the AuNR core was recovered. As a part of this study, we also synthesized Ag_2S - and Ag_2Se -coated AuNRs as negative controls (E^0 of $\text{Ag}_2\text{S}(\text{s}) + 2\text{e}^- \rightarrow 2\text{Ag}(\text{s}) + \text{S}^{2-}(\text{aq}) = -0.69$ V) that show no etching in the presence of HCF or RONS.⁴⁰ The negative reduction potential of silver chalcogenides means that Ag is already oxidized and cannot be oxidized further using HCF. Indeed, we observed no etching of the silver chalcogenide shell and no change in the LSPR upon HCF treatment but observed a ~40-fold PA enhancement. The PA enhancement is interesting because traditionally an increase in absorption (μ_a) at the imaging wavelength results in PA enhancement.¹ Surprisingly, these silver chalcogenide-coated AuNRs showed no change in absorbance after HCF treatment but a much higher PA signal. Thus, the goal of this work was to study the interaction between HCF and the nanoparticle surface to elucidate the mechanism underlying this surprising PA enhancement.

METHODS

Materials.

Hexadecyltrimethylammonium bromide (CTAB, Cat. #1102974), L-ascorbic acid (Cat. #255564), silver nitrate (Cat. #209139), potassium HCF(III) (Cat. #244023), gold(III) chloride trihydrate (Cat. #520918), selenourea (Cat. #230499), and titanium(IV) oxide (Cat. #718467) were purchased from Sigma-Aldrich (Atlanta, GA, USA). Sodium borohydride (Cat. #S678-25) and sodium hydroxide (Cat. #1310-73-2) were purchased from Fisher Scientific (Pittsburgh, PA, USA). Sodium sulfide (Cat. #65122-06) was purchased from Alfa Aesar (Tewksbury, MA, USA). All chemicals were used as received without further purification.

Nanoparticle Synthesis.

CTAB-stabilized AuNRs were synthesized using a seed-mediated growth method reported previously.¹⁰ Gold seeds were synthesized by adding 5 mL of CTAB (0.2 M) to 2.5 mL of HAuCl₄·3H₂O (0.001 M); 0.6 mL of ice-cold NaBH₄ (0.01 M) was used as a reducing agent under vigorous stirring for 2 min. The growth solution was a mixture of 500 mL of HAuCl₄·3H₂O (0.001 M) and 500 mL of CTAB (0.2 M). Next, 7 mL of L-ascorbic acid (0.089 M) and 36 mL of AgNO₃ (0.004 M) were added to the growth solution. The color of the solution turned from dark orange to colorless. Finally, 1.2 mL of the seed solution was added, and the reaction mixture was hand swirled for 5 s. The reaction vessel was left undisturbed for 12 h as the solution turned purple/dark brown. The AuNRs were washed thrice via centrifugation at 12,500 rpm for 15 min each and stored at 4 °C; the stock concentration was 9.35 nM. All experiments were carried out using the same batch of AuNRs.

The silver chalcogenide coating of AuNRs was done in a two-step process (Figure 1A).⁴⁰ AuNRs were first coated with a silver shell.¹⁰ Next, 0.48 mL of AuNRs (9.35 nM) was diluted in a mixture of 12 mL of water and 2 mL of CTAB (0.1 M). To this, we added 0.36 mL of AgNO₃ (0.010 M), 0.34 mL of L-ascorbic acid (0.1 M), and 0.84 mL of NaOH (0.1 M). The reaction was vigorously stirred for 30 min as the color changed from pink to dark green. The resulting silver-coated AuNRs (Ag/AuNRs) were doped with 0.36 mL of Na₂S (0.010 M) or SeC(NH₂)₂ (0.010 M) under vigorous stirring for 2 h while open to air. The Na₂S and SeC(NH₂)₂ doping results in the formation of Ag₂S/AuNR and Ag₂Se/AuNR, respectively. Nanoparticles were further purified via centrifugation at 12,500 rpm for 15 min and dispersed in water. CTAB, Na₂S, and SeC(NH₂)₂ are all corrosive, toxic, and an environmental hazard and should be used with care with full personal protective equipment. The synthesized nanoparticles themselves are not toxic.

Nanoparticle Characterization.

Absorption Spectroscopy.—All optical absorption spectra were acquired using the BioTek Synergy H1 microplate reader from Agilent (Santa Clara, CA, USA). We used 150 μ L of the solution in a 96-well plate. Unless otherwise mentioned, absorption spectra were acquired between 280 and 995 nm with a step size of 5 nm.

Dynamic Light Scattering and Zeta Potential.—Dynamic light scattering (DLS) and zeta potential were measured using a Malvern Instruments Zetasizer ZS 90; 0.2 mL of the particles was diluted in 0.8 mL of water.

Transmission Electron Microscopy and Energy-Dispersive X-ray

Spectroscopy.—All high-resolution electron micrographs [high-resolution transmission electron microscopy (HR-TEM); mag: 650,000 \times] and energy-dispersive X-ray spectroscopy (EDX) maps were acquired using a Thermo Fisher Talos 200X system at an operating voltage of 200 kV. Low-magnification (mag: 150,000 \times) TEM images were acquired on a JEOL JEM-1400Plus system operating at 80 kV. Images were recorded using a Gatan OneView 4K digital camera.

Powder X-ray Diffraction.—Powder X-ray diffraction (pXRD) was performed using a Bruker D8 ADVANCE operating in Bragg–Brentano geometry. Cu radiation: 1.54 Å, equipped with a Ni K β filter. The 2θ scan range was 10–80° with a step size of 0.02° and an exposure of 0.25 s. Samples were prepared by concentrating 1 mL of the synthesized nanoparticles to 0.02 mL via centrifugation and then redispersing in distilled water.

Attenuated Total Reflectance–Fourier Transform Infrared Spectroscopy.—A more detailed description of the attenuated total reflectance–Fourier transform infrared (ATR–FTIR) spectroscopy setup can be found elsewhere.^{41,42} Infrared spectra were collected using a Nicolet iS10 Fourier transform infrared spectrophotometer with a mercury cadmium telluride detector. Spectra were averaged over 100 scans with a 4 cm⁻¹ resolution over the spectral range from 750 to 4000 cm⁻¹; OMNIC 9 software was used to collect data. The software was also used for background subtractions and baseline corrections. For solution-phase spectra, samples were pipetted onto the AMTIR crystal and covered. The chamber was purged with dry air to remove atmospheric gases for approximately 30 min before each spectrum was collected. All in situ spectroscopic measurements involved collecting spectra every 2.5 min during an aqueous flow over the sample as described below.

For dynamic in situ measurements, a dry nanoparticle thin film was first created by drop-casting 1 mL of a ~27 nM nanoparticle concentration onto the crystal and dried overnight with a continuous dry air purge. For displacement reactions on silver chalcogenide-coated AuNRs, water was flowed at ~1 mL/min for 60 min to remove loose particles, followed by a background scan. Next, 50 μ M HCF was flowed over the film for 90 min, and another scan was taken. Then, 50 μ M CTAB was flowed over the thin film for 90 min, and another scan was taken. Finally, for desorption, water was flowed over the film for 60 min.

For displacement reactions on the AuNR, a dried particle film was created by drop-casting 1 mL of ~27 nM particles onto the AMTIR crystal and dried overnight. The water background, HCF adsorption, CTAB displacement, and water desorption were similarly performed as previously mentioned but at ~0.2 mL/min. The flow rate was reduced to minimize film dewetting on the AMTIR crystal because the AuNR thin film was less stable on the AMTIR crystal compared to the silver chalcogenide-coated AuNRs.

PA Imaging.—All PA images were acquired using the Visualsonics Vevo 2100 LAZR from Fujifilm Visualsonics Inc. (Toronto, Canada). Images were acquired at 710 nm, with a pulse width of 4–6 ns, using the LZ250 transducer, $F_c = 21$ MHz. The PA spectrum was acquired between 680 and 970 nm with a step size of 2 nm.

PA enhancement was initiated using potassium HCF(III). Silver chalcogenide-coated AuNRs were washed twice via centrifugation at 12,500 rpm for 5 min and redispersed in distilled water to remove excess CTAB. Next, 50 μM HCF was added to initiate PA enhancement. All HCF-treated characterizations were done using the same batch of particles treated with 50 μM HCF. Note that HCF itself has low toxicity but can release HCN gas in an acidic medium and should be handled with extra care.

The Grüneisen parameter was measured by controlling the sample temperature between 6 and 45 °C. The slope of the PA intensity versus sample temperature reports the Grüneisen parameter.^{43–45} Particle photostability was measured by monitoring the PA intensity under 7 min of laser illumination. The effect of laser fluence on PA signal generation was studied using agarose-TiO₂ nanoparticle filters as described previously.⁴⁶ Nine agarose-TiO₂ optical filters ranging from 0 to 8 mg/mL TiO₂ were used to modulate the laser fluence on the sample. The laser fluence was measured using a laser pyroelectric energy sensor (PE50BF-C, Ophir LLC, USA).

Data Processing.—PA, EDX, and TEM images were processed using ImageJ version 2.1.0/1.53c using the region of interest analysis (ROI). All data were plotted using GraphPad Prism 9.3.1 (350).

RESULTS AND DISCUSSION

The figures in this section focus on the Ag₂S/AuNR. Characterization and PA data on the Ag₂Se/AuNR can be found in the Supporting Information.

Nanoparticle Synthesis and Characterization.

The AuNRs were synthesized using a seed-mediated method.¹⁰ The AuNR aspect ratio was 3.08 ± 0.35 ($n > 100$ particles) with a peak absorbance of 710 nm (Figure 1B,E). HR-TEM and pXRD confirmed the characteristic 111, 200, 220, and 311 Au crystal facets (JCPDS 04-0784, Figure 1H).^{47,48} DLS showed two peaks at 1.2 and 50.7 nm. DLS inherently assumes that all particles are spherical and hence not ideal to the size of rod-like particles. The 1.2 nm peak can be attributed to the rotational diffusion coefficient of AuNRs.¹⁰

Coating with chalcogenides results in a core–shell nanostructure (Figures 1C and S1A) with a visible color change from pale pink AuNRs to green Ag₂S/Se-coated AuNRs (Figures 1D and S1C). The Ag₂S/AuNR and Ag₂Se/AuNR had a shell thickness of 7.3 ± 1.4 and 6.6 ± 1.5 nm, respectively. DLS showed an increase in the particle's hydrodynamic diameter to 8.1 and 7.6 nm for Ag₂S/AuNR and Ag₂Se/AuNR, respectively (Figures 1I and S1E). The absorption spectra were attenuated and red-shifted after coating (Figures 1E and S1C). The degree of red-shifting and the degree of attenuation depend on the shell thickness and the high refractive index of the silver chalcogenide shell, respectively.⁴⁰ The EDX mapping of

Ag₂S/AuNR shows a gold nanorod core surrounded by a silver sulfide shell (Figure 1F,G). pXRD analysis after shell coating showed characteristic crystal facets for Au, Ag₂S, and Ag₂Se (JCPDS 04-0784, 14-0072, and 24-1041, respectively).

HCF-Mediated PA Enhancement.

Here, the 50 μ M HCF treatment has no significant effect on the absorption spectra of silver chalcogenide-coated AuNRs (Figures 2A and S1C). Conventional wisdom dictates that no change in absorbance should result in no PA change.¹ However, the HCF treatment of Ag₂S- and Ag₂Se-coated AuNRs results in an uncharacteristic 42- and 27-fold PA enhancement, respectively (Figures 2C and S2B). Furthermore, the PA spectrum shows enhanced PA in the NIR region (Figures 2D and S2C), whereas absorbance is lowest in the 700–800 nm range. The bare AuNRs showed no significant change in absorbance or PA enhancement upon HCF treatment (Figures S3 and S4). The PA enhancement was specific to rod-shaped particles. Ag₂S-coated gold spheres (AuSph) showed no change in absorbance or PA intensity after HCF addition (Figure S5).

The Grüneisen parameter (Γ , eq 1) characterizes the thermo-acoustic conversion efficiency. Γ is directly proportional to the particle's β .²⁰ Up to 93% of the PA signal generation can occur in the solvent surrounding the particle.³ Others have reported the use of different solvents to modulate the PA intensity of gold nanoparticles.^{14,43,49} Water is a unique solvent to decouple the PA signal generated by the particle from the PA signal generated by the solvent. β of pure water tends to 0 at 3.98 °C.⁵⁰ Hence, the PA signal from water disappears at that temperature, thus allowing one to isolate the PA signal from the nanoparticle. The slope of the curve plotting the PA intensity versus temperature indirectly reports Γ of the nanoparticle. Uncoated AuNRs exhibit a characteristic PA behavior with water at low temperatures (Figure S4D). HCF treatment causes no significant change in the AuNR's Γ value ($p > 0.05$); both samples show zero PA signal in the 0–4 °C range. The slight deviation from 3.98 °C can be attributed to impurities such as excess CTAB and HCF in solution. Ag₂S/AuNRs show a unique PA response to changes in temperature (Figure 3A,B). Untreated nanoparticles have a low but linear PA response with zero PA signal at 10.8 °C. On the other hand, HCF-treated Ag₂S/AuNRs show an enhanced PA response with a 4-fold higher Γ value ($p < 0.001$) and zero PA signal at –12.4 °C. The nonzero PA signal at 4 °C after HCF addition suggests that the PA enhancement is due to increased thermal confinement within the core–shell nanoparticle and is independent of the solvent. Coatings such as silica and polydimethylsiloxane have also shown thermal confinement effects on gold nanoparticles.^{20,27}

The laser fluence (F , eq 1) is directly proportional to the PA intensity. We controlled the laser fluence using a 1 cm thick agarose-based TiO₂ (0–8 mg/mL) filter as an optical scatterer.⁴⁶ Figure S4A shows the experimental setup to control laser fluence. HCF treatment had no effect on the linear response of AuNRs (Figure S4B). Silver chalcogenide-coated rods also showed a strong linear correlation between the PA intensity and laser fluence (Figure S4C,D) on HCF treatment. Particles not treated with HCF showed low correlation, but this is attributed to extremely low PA intensity across all laser fluences. The higher PA intensity of HCF-treated Ag₂S/Se/AuNRs at lower fluence could have applications for

an LED-based PA system. LED-based systems are cheaper and more robust but operate at a ~ 1000 -fold lower fluence.⁵¹ Low fluence means that more concentrated contrast agents are required to generate the same amount of contrast. Hence, engineering materials with enhanced PA contrast is extremely important. Photostability is also improved (6.5 and 9% decrease in the PA intensity for S and Se, respectively) when irradiated at the highest fluence of 18.2 ± 0.9 mJ/pulse for over 7 min (Figure S5). In contrast, the low photostability of uncoated AuNRs is evident with 62% decrease in PA intensity. AuNRs are known to melt into more thermodynamically favorable spheres under high-fluence irradiation.^{1,52}

Nanoparticle Characterization after HCF Treatment.

PA enhancement can be driven by nanoparticle aggregation.¹ Aggregation can cause changes in absorbance or increase the thermal flux in the solvent.²⁶ An increase in absorbance further enhances the PA intensity. HCF treatment does not result in aggregation of coated or uncoated nanorods as seen in the TEM images, absorption spectra, and size distribution via DLS (Figures 4, S1, and S3). Therefore, aggregation or changes in optical absorption was excluded as a mechanism for the enhancement seen here. In our previous work with Ag/AuNRs, the Ag shell was selectively etched off using HCF as a positive control.¹¹ The shell etching resulted in a AuNR LSPR recovery and PA signal increase. With Ag₂S- and Ag₂Se-coated AuNRs, the TEM images (Figures 4 and S1) indicate that the shell layer remains unetched after HCF treatment. Ag in the shell is already in the oxidized state due to the chalcogenides and hence cannot be oxidized further using HCF. This makes the Ag₂S- and Ag₂Se-coated AuNRs stable against HCF. Since the particle morphology is conserved, there is no change in absorption spectra. Hence, change in the nanoparticle morphology was ruled out.

A high β of the material increases the PA signal.¹ Importantly, different phases of crystals are known to have different β values. In our system, nanocrystalline Ag₂S can have three major phases: monoclinic acanthite (α -Ag₂S), body-centered cubic argentite (β -Ag₂S), and face-centered cubic phases (γ -Ag₂S). α -Ag₂S is more common under ambient conditions; β - and γ -Ag₂S are stable at 456 and 865 K, respectively.⁵³ β -Ag₂S has the highest thermal expansion coefficient of the three phases.⁵³ We did not heat the nanoparticles to those temperatures, but others have shown that a phase transition in metal chalcogenides is possible via chemical modification.⁵⁴ For example, *n*-butyllithium-treated MoS₂ was reported to undergo a phase change due to the electrons injected by *n*-butyllithium treatment occupying the lowest energy states above the Fermi energy.⁵⁴ Thus, it is plausible that the HCF treatment causes a phase change in our system, an increase in β , and thus an increase in the PA signal. However, we did not observe any change in the crystal structure upon HCF addition (Figures 4H, S1D, and S3D) in any of our particles. Hence, this hypothesis was rejected.

Another hypothesis is that HCF displaces CTAB on the particle surface. CTAB is a positively charged surfactant commonly used to stabilize AuNRs.^{55,56} HCF is a negatively charged molecule; hence, the substitution of CTAB with HCF should change the particle's surface charge. There is a significant reduction ($p < 0.05$) in the zeta potential for all particles as the negatively charged [Fe(CN)₆]³⁻ gets adsorbed onto the particle surface. The

dynamic interaction between HCF and CTAB on the particle surface was further studied using ATR–FTIR (Figures 5, S9, S12, and S13). The experimental setup is illustrated in Figure S8.

Figures 5A and S12A show the dried thin film spectra of the CTAB-stabilized Ag₂S/AuNR and Ag₂Se/AuNR, respectively. Significant $\nu(\text{C–H})$ vibrations at 2917 and 2849 cm⁻¹ from methyl and methylene groups from CTAB coatings, respectively, are observed for both particles. The particles also had a strong positive zeta potential before HCF addition due to CTAB stabilization.⁵⁶ This suggests that a large amount CTAB was present in the colloidal suspension and that CTAB remained on the film when the suspension was dried. For the in situ temporal adsorption spectra, water was initially flowed over the film to remove excess CTAB and loose particles (Figure S9A). CTAB-related peaks decreased with minimal peak shifts, thus indicating the removal of excess CTAB only. Flowing water for 60 min results in a plateau for changes in the CTAB peak intensity; the maximum amount of CTAB is removed from the particle surface at this point (Figure S9B).

Figure 5B shows the in situ ATR–FTIR spectra as HCF, CTAB, and water are flowed across the nanorod film (three consecutive flow streams after the initial water wash). The 2044 cm⁻¹ peak appears as HCF flowed over the Ag₂S/AuNR thin film, while CTAB $\nu(\text{C–H})$ 2917 and 2849 cm⁻¹ decrease (Figure 5B(i)). This suggests that HCF has a higher affinity for the nanoparticle surface and displaces CTAB. Solution-phase 50 μM HCF has negligible spectral absorbance values and minimally contributes to the adsorbed intensity (data not shown).

Surface interactions were determined using the 1 mM HCF solution-phase spectra (Figure 5A) as a reference. The 2115 cm⁻¹ peak for the 1 mM HCF solution phase is assigned to the $\nu(\text{C}\equiv\text{N})$ vibration mode. The 2044 cm⁻¹ peak appears when HCF is adsorbed onto the Ag₂S/AuNR. In contrast to the 2115 cm⁻¹ solution-phase peak, the adsorbed 2044 cm⁻¹ peak is broader and shifts to a lower peak position, thus indicating that HCF complexes with the surface.

Solution-phase HCF is a centrosymmetric molecule, and when adsorbed onto the nanorod surface, the symmetry changes and new peaks appear.⁵⁷ The interaction with the surface also leads to the broadening of the infrared peaks. The adsorption of HCF is further corroborated with the EDX spectra, thus showing Fe adsorption after HCF treatment (Figure 4F). EDX is a surface-weighted technique and cannot decipher between passive adsorption and complexation between HCF and a Ag-chalcogenide. Previous studies also report strong interactions of ferro- and ferri-cyanide ions adsorbing onto Ag electrodes via a Ag–C \equiv N interaction.⁵⁸ At earlier time points and subsequently low surface coverage, the initially adsorbed HCF peak appears at 2044 cm⁻¹. The peak shifts to 2057 cm⁻¹ at higher surface coverage. The peak shift with the increase of adsorption time could suggest a surface concentration-dependent interaction with the Ag₂S/AuNR surface. Hence, there is a strong positive correlation between the PA amplitude and HCF concentration (Figure 2B).

Following the adsorption of HCF, CTAB was flowed over the film to observe any reversible displacement reactions (Figure 5B(ii)). Positive peaks at 2926 and 2854 cm⁻¹ are now

observed to increase in intensities and are assigned to CTAB $\nu(\text{C-H})$. Interestingly, the 2926 and 2824 cm^{-1} peaks more closely resemble solution-phase CTAB but are different from the displaced peak positions at 2917 and 2854 cm^{-1} when flowed with HCF. This suggests that CTAB forms a multilayer on top of HCF rather than interacting directly with the $\text{Ag}_2\text{S}/\text{AuNR}$ surface, supporting the fact that HCF has a higher affinity to the surface than CTAB. As the CTAB layer grows on top of HCF, PA enhancement is steadily lost (Figure S10). A slight decrease in the 2038 cm^{-1} HCF peak is observed and could be due to the desorption of loosely bound HCF. Additionally, the $\nu(\text{C}\equiv\text{N})$ peak shape narrowed, and the position shifted from 2057 to 2038 cm^{-1} when CTAB was flowed over the HCF-adsorbed film. Introducing CTAB into the aqueous flow caused multilayer interactions between HCF and CTAB. When particles are washed via centrifugation instead of CTAB to remove the adsorbed HCF, the pellet still shows PA enhancement. The supernatant shows no PA contrast (Figure S11).

When the thin film is desorbed with pure water (Figure 5B(iii)), there is a drastic decrease in the $\nu(\text{C-H})$ 2926 and 2854 cm^{-1} peak intensities, indicating that the multilayer CTAB is reversibly adsorbed. HCF also desorbs, as noted by the decrease in peak intensities. Peak broadening is also seen, suggesting low surface coverage conditions.

Similar analyses can be made with the $\text{Ag}_2\text{Se}/\text{AuNR}$ (Figure S12). When the film is flowed with HCF, the surface-complexed HCF 2049 cm^{-1} peak appears, while a loosely bound CTAB is displaced. With the CTAB and water desorption flow streams, HCF-related peaks can be seen to decrease, indicating partial desorption. Multilayer reversible CTAB adsorption is observed with the $\nu(\text{C-H})$ peak positions resembling solution-phase positions and with intensities falling to baseline values. When comparing the adsorbed HCF spectra between the $\text{Ag}_2\text{S}/\text{AuNR}$ and $\text{Ag}_2\text{Se}/\text{AuNR}$, varying surface complexation modes are seen, as noted by the HCF peak position and broadening. This suggests that the surface complexation mode is dependent on the nanoparticle composition and surface coverage. The slight desorption of HCF from $\text{Ag}_2\text{Se}/\text{AuNRs}$ (27-fold) could explain the lower PA enhancement compared to that from $\text{Ag}_2\text{S}/\text{AuNRs}$ (42-fold).

Bare AuNRs show minimal adsorption of HCF and CTAB (Figure S13). When water is finally flowed over the AuNRs, all molecules are completely desorbed, thus suggesting a fully reversible physisorption process. Thus, HCF is directly complexed with the chalcogenide coating and not the core gold nanorod. This explains why AuNRs treated with HCF show no PA enhancement (Figure S6).

EDX mapping shows a slight preferential adsorption of HCF along the longitudinal edge of the nanoparticle surface (Figure 4F,G). This could explain why $\text{Ag}_2\text{S}/\text{AuSph}$ shows no PA enhancement compared to the coated nanorods (Figure S5). PA enhancement was specific to HCF(III). 50 μM potassium ferrocyanide [HCF(II)], KO_2 , NaCN, NaH, and KMnO_4 had no effect on the PA signal from the $\text{Ag}_2\text{S}/\text{AuNR}$ (Figure S14).

There are two possible hypotheses for how HCF adsorption causes an increase in the Grüneisen parameter (Γ). Γ is a temperature-dependent variable. Recently, HCF was associated with excess heat production during a redox couple reaction.⁵⁹ It is also well known that HCF redox can be triggered by light absorption like the kind used in PAs.^{60,61}

Hence, it is possible that HCF adsorption and subsequent light absorption increase the temperature at the shell–HCF interface, resulting in a 4-fold Γ enhancement.

Second, there could be enhanced electrostriction due to HCF adsorption. Electrostriction is a material property that results in a rapid shape change in the presence of an externally applied electric field.⁶² An external electric field can displace electron–hole pairs in opposite directions, resulting in a bulk volumetric change.⁶³ Γ is directly proportional to the volumetric thermal expansion coefficient (β , eq 1).⁶⁴ An increase in β will result in enhanced Γ . In the case of plasmonic nanoparticles, the excitation from the pulsed light source can result in rapid shape changes. PA generated from electrostriction and thermal expansion of the particle would be additive and result in PA enhancement. Usually, the electrostriction forces are negligible and hence excluded from eq 1.^{65,66} However, others have shown that ferricyanide, chalcogenophosphates, and layered materials can possess enhanced electrostriction properties.^{65,67–69} PA imaging is one of the best ways to characterize both these hypotheses, and an independent characterization technique is needed to confirm our findings. Unfortunately, independent confirmation is extremely challenging due to instrument limitations. The ability to engineer contrast agents with PA enhancement will help the community better understand the PA effect. This in turn will help design more efficient and clinically translatable contrast agents.

CONCLUSIONS

In this work, we report the surprising PA enhancement of silver chalcogenide-coated AuNRs upon treatment with HCF. HCF-treated nanoparticles showed no changes in absorbance but a significant (up to 42-fold) PA enhancement. $\text{Ag}_2\text{S}/\text{AuNRs}$ showed higher PA efficiency compared to $\text{Ag}_2\text{Se}/\text{AuNRs}$. AuSph showed no PA enhancement. The PA enhancement was attributed to a 4-fold increase in the Grüneisen parameter (Γ) after HCF addition. We showed that the Γ enhancement was not due to aggregation, increased absorbance, or crystal phase change of the shell layer. Dynamic in situ interactions between HCF and the silver chalcogenide surface revealed the irreversible displacement of CTAB with HCF from the nanoparticle shell surface. Uncoated AuNRs showed minimal HCF adsorption resulting in no Γ enhancement. We include two possible mechanisms for Γ enhancement: first, the localized heating at the shell–HCF interface due to photo-induced HCF redox chemistry. Since Γ is temperature-dependent, localized heating results in Γ enhancement. Second, there may be an enhanced electrostriction response due to ferricyanide adsorption on a layered plasmonic nanoparticle surface which increases the volumetric thermal expansion component of Γ .

Supplementary Material

Refer to Web version on PubMed Central for supplementary material.

ACKNOWLEDGMENTS

The TOC figure, Figures 1A, S4A, S8, and S11A were made using [BioRender.com](https://www.biorender.com). We acknowledge funding from the National Institutes of Health (NIH) through grant S10 OD021821. The low-resolution TEM images were acquired at the UCSD Cellular and Molecular Medicine Electron Microscopy Core Facility (UCSD-CMM-EM Core, RRID:SCR_022039) which is supported in part by the NIH award S10 OD023527. The HR-TEM and

EDX images were acquired at the San Diego Nanotechnology Infrastructure (SDNI) at UCSD, a member of the National Nanotechnology Coordinated Infrastructure, which is supported by the National Science Foundation (Grant ECCS-2025752).

REFERENCES

- (1). Mantri Y; Jokerst JV Engineering Plasmonic Nanoparticles for Enhanced Photoacoustic Imaging. *ACS Nano* 2020, 14, 9408–9422. [PubMed: 32806027]
- (2). Manohar S; Ungureanu C; Van Leeuwen TG Gold Nanorods as Molecular Contrast Agents in Photoacoustic Imaging: The Promises and the Caveats. *Contrast Media Mol. Imaging* 2011, 6, 389–400. [PubMed: 22025339]
- (3). Shahbazi K; Frey W; Chen Y-S; Aglyamov S; Emelianov S Photoacoustics of Core–Shell Nanospheres Using Comprehensive Modeling and Analytical Solution Approach. *Commun. Phys* 2019, 2, 119.
- (4). Knights OB; Ye S; Ingram N; Freear S; McLaughlan JR Optimising Gold Nanorods for Photoacoustic Imaging in Vitro. *Nanoscale Adv.* 2019, 1, 1472–1481. [PubMed: 36132606]
- (5). Lohse SE; Murphy CJ The Quest for Shape Control: A History of Gold Nanorod Synthesis. *Chem. Mater* 2013, 25, 1250–1261.
- (6). Dhada KS; Hernandez DS; Suggs LJ In Vivo Photoacoustic Tracking of Mesenchymal Stem Cell Viability. *ACS Nano* 2019, 13, 7791–7799. [PubMed: 31250647]
- (7). Guo D; Huang Y; Jin X; Zhang C; Zhu X A Redox-Responsive, in-Situ Polymerized Polyplatinum (Iv)-Coated Gold Nanorod as an Amplifier of Tumor Accumulation for Enhanced Thermo-Chemotherapy. *Biomaterials* 2021, 266, 120400. [PubMed: 33022477]
- (8). Jokerst JV; Cole AJ; Van de Sompel D; Gambhir SS Gold Nanorods for Ovarian Cancer Detection with Photoacoustic Imaging and Resection Guidance Via Raman Imaging in Living Mice. *ACS Nano* 2012, 6, 10366–10377. [PubMed: 23101432]
- (9). Li P-C; Wei C-W; Liao C-K; Chen C-D; Pao K-C; Wang C-RC; Wu Y-N; Shieh D-B Photoacoustic Imaging of Multiple Targets Using Gold Nanorods. *IEEE Trans. Sonics Ultrason* 2007, 54, 1642–1647.
- (10). Mantri Y; Davidi B; Lemaster JE; Hariri A; Jokerst JV Iodide-Doped Precious Metal Nanoparticles: Measuring Oxidative Stress in Vivo Via Photoacoustic Imaging. *Nanoscale* 2020, 12, 10511–10520. [PubMed: 32396928]
- (11). Kim T; Zhang Q; Li J; Zhang L; Jokerst JV A Gold/Silver Hybrid Nanoparticle for Treatment and Photoacoustic Imaging of Bacterial Infection. *ACS Nano* 2018, 12, 5615–5625. [PubMed: 29746090]
- (12). Cavigli L; Centi S; Borri C; Tortoli P; Panettieri I; Streit I; Ciofini D; Magni G; Rossi F; Siano S; Ratto F; Pini R 1064-Nm-Resonant Gold Nanorods for Photoacoustic Theranostics within Permissible Exposure Limits. *J. Biophotonics* 2019, 12, No. e201900082. [PubMed: 31155855]
- (13). Xu M; Wang LV Photoacoustic Imaging in Biomedicine. *Rev. Sci. Instrum* 2006, 77, 041101.
- (14). Chen Y-S; Frey W; Aglyamov S; Emelianov S Environment-Dependent Generation of Photoacoustic Waves from Plasmonic Nanoparticles. *Small* 2012, 8, 47–52. [PubMed: 22114029]
- (15). Luke GP; Yeager D; Emelianov SY Biomedical Applications of Photoacoustic Imaging with Exogenous Contrast Agents. *Ann. Biomed. Eng* 2012, 40, 422–437. [PubMed: 22048668]
- (16). Xu M; Yim W; Zhou J; Zhou J; Jin Z; Moore C; Borum R; Jorns A; Jokersta JV The Application of Organic Nanomaterials for Bioimaging, Drug Delivery, and Therapy: Spanning Various Domains. *IEEE Nanotechnol.Mag* 2021, 15, 8.
- (17). Weber J; Beard PC; Bohndiek SE Contrast Agents for Molecular Photoacoustic Imaging. *Nat. Methods* 2016, 13, 639–650. [PubMed: 27467727]
- (18). Fu Q; Zhu R; Song J; Yang H; Chen X Photoacoustic Imaging: Contrast Agents and Their Biomedical Applications. *Adv. Mater* 2019, 31, 1805875.
- (19). Upputuri PK; Pramanik M Recent Advances in Photoacoustic Contrast Agents for in Vivo Imaging. *Wiley Interdiscip. Rev.: Nanomed. Nanobiotechnol* 2020, 12, No. e1618. [PubMed: 32027784]

- (20). Shi Y; Qin H; Yang S; Xing D Thermally Confined Shell Coating Amplifies the Photoacoustic Conversion Efficiency of Nanoprobes. *Nano Res.* 2016, 9, 3644–3655.
- (21). Masim FCP; Hsu W-H; Liu H-L; Yonezawa T; Bal ytis A; Juodkakis S; Hatanaka K Photoacoustic Signal Enhancements from Gold Nano-Colloidal Suspensions Excited by a Pair of Time-Delayed Femtosecond Pulses. *Opt. Express* 2017, 25, 19497–19507. [PubMed: 29041143]
- (22). Zhong J; Wen L; Yang S; Xiang L; Chen Q; Xing D Imaging-Guided High-Efficient Photoacoustic Tumor Therapy with Targeting Gold Nanorods. *Nanomedicine* 2015, 11, 1499–1509. [PubMed: 25933697]
- (23). Khanal A; Ullum C; Kimbrough CW; Garbett NC; Burlison JA; McNally MW; Chuong P; El-Baz AS; Jasinski JB; McNally LR Tumor Targeted Mesoporous Silica-Coated Gold Nanorods Facilitate Detection of Pancreatic Tumors Using Multi-spectral Photoacoustic Tomography. *Nano Res.* 2015, 8, 3864–3877.
- (24). Huff TB; Tong L; Zhao Y; Hansen MN; Cheng J-X; Wei A Hyperthermic Effects of Gold Nanorods on Tumor Cells. *Nanomedicine* 2007, 2, 125–132. [PubMed: 17716198]
- (25). Chen J; Liang H; Lin L; Guo Z; Sun P; Chen M; Tian H; Deng M; Chen X Gold-Nanorods-Based Gene Carriers with the Capability of Photoacoustic Imaging and Photothermal Therapy. *ACS Appl. Mater. Interfaces* 2016, 8, 31558–31566. [PubMed: 27775317]
- (26). Bayer CL; Nam SY; Chen Y-S; Emelianov SY Photoacoustic Signal Amplification through Plasmonic Nanoparticle Aggregation. *J. Biomed. Opt* 2013, 18, 016001.
- (27). Chen Y-S; Frey W; Kim S; Kruizinga P; Homan K; Emelianov S Silica-Coated Gold Nanorods as Photoacoustic Signal Nanoamplifiers. *Nano Lett.* 2011, 11, 348–354. [PubMed: 21244082]
- (28). Jokerst JV; Thangaraj M; Kempen PJ; Sinclair R; Gambhir SS Photoacoustic Imaging of Mesenchymal Stem Cells in Living Mice Via Silica-Coated Gold Nanorods. *ACS Nano* 2012, 6, 5920–5930. [PubMed: 22681633]
- (29). Yim W; Borum RM; Zhou J; Mantri Y; Wu Z; Zhou J; Jin Z; Creyer M; Jokerst JV Ultrasmall Gold Nanorod-Polydopamine Hybrids for Enhanced Photoacoustic Imaging and Photothermal Therapy in Second near-Infrared Window. *Nanotheranostics* 2022, 6, 79–90. [PubMed: 34976582]
- (30). Yim W; Zhou J; Mantri Y; Creyer MN; Moore CA; Jokerst JV Gold Nanorod–Melanin Hybrids for Enhanced and Prolonged Photoacoustic Imaging in the near-Infrared-II Window. *ACS Appl. Mater. Interfaces* 2021, 13, 14974–14984. [PubMed: 33761255]
- (31). He L; Mao C; Brasino M; Harguindey A; Park W; Goodwin AP; Cha JN Tio₂-Capped Gold Nanorods for Plasmon-Enhanced Production of Reactive Oxygen Species and Photothermal Delivery of Chemotherapeutic Agents. *ACS Appl. Mater. Interfaces* 2018, 10, 27965–27971. [PubMed: 30044085]
- (32). Moon H; Kumar D; Kim H; Sim C; Chang J-H; Kim J-M; Kim H; Lim D-K Amplified Photoacoustic Performance and Enhanced Photothermal Stability of Reduced Graphene Oxide Coated Gold Nanorods for Sensitive Photoacoustic Imaging. *ACS Nano* 2015, 9, 2711–2719. [PubMed: 25751167]
- (33). Cavigli L; Milanesi A; Khlebtsov BN; Centi S; Ratto F; Khlebtsov NG; Pini R Impact of Kapitza Resistance on the Stability and Efficiency of Photoacoustic Conversion from Gold Nanorods. *J. Colloid Interface Sci* 2020, 578, 358–365. [PubMed: 32535418]
- (34). Pang GA; Poisson F; Laufer J; Haisch C; Bossy E Theoretical and Experimental Study of Photoacoustic Excitation of Silica-Coated Gold Nanospheres in Water. *J. Phys. Chem. C* 2019, 124, 1088–1098.
- (35). Gao F; Bai L; Liu S; Zhang R; Zhang J; Feng X; Zheng Y; Zhao Y Rationally Encapsulated Gold Nanorods Improving Both Linear and Nonlinear Photoacoustic Imaging Contrast in Vivo. *Nanoscale* 2017, 9, 79–86. [PubMed: 27911452]
- (36). Nguyen SC; Zhang Q; Manthiram K; Ye X; Lomont JP; Harris CB; Weller H; Alivisatos AP Study of Heat Transfer Dynamics from Gold Nanorods to the Environment Via Time-Resolved Infrared Spectroscopy. *ACS Nano* 2016, 10, 2144–2151. [PubMed: 26840805]
- (37). Wang Y; Zhan Y; Harris LM; Khan S; Xia J A Portable Three-Dimensional Photoacoustic Tomography System for Imaging of Chronic Foot Ulcers. *Quant. Imag. Med. Surg* 2019, 9, 799.

- (38). Moore C; Jokerst JV Strategies for Image-Guided Therapy, Surgery, and Drug Delivery Using Photoacoustic Imaging. *Theranostics* 2019, 9, 1550. [PubMed: 31037123]
- (39). Doronin SV; Manzhos RA; Krivenko AG Edl Structure and Peculiarities of Ferricyanide Cyclic Voltammetry for Silver Deposits on Gold. *Electrochem. Commun* 2015, 57, 35–38.
- (40). Liu M; Guyot-Sionnest P Preparation and Optical Properties of Silver Chalcogenide Coated Gold Nanorods. *J. Mater. Chem* 2006, 16, 3942–3945.
- (41). Sit I; Wu H; Grassian VH Environmental Aspects of Oxide Nanoparticles: Probing Oxide Nanoparticle Surface Processes under Different Environmental Conditions. *Annu. Rev. Anal. Chem* 2021, 14, 489–514.
- (42). Sit I; Sagisaka S; Grassian VH Nucleotide Adsorption on Iron (Iii) Oxide Nanoparticle Surfaces: Insights into Nano-Geo-Bio Interactions through Vibrational Spectroscopy. *Langmuir* 2020, 36, 15501–15513. [PubMed: 33331787]
- (43). Villanueva Y; Hondebrink E; Petersen W; Steenbergen W Photoacoustic Measurement of the Gruneisen Parameter Using an Integrating Sphere. *Rev. Sci. Instrum* 2014, 85, 074904. [PubMed: 25085163]
- (44). Mallidi S; Emelianov S Photoacoustic Technique to Measure Beam Profile of Pulsed Laser Systems. *Rev. Sci. Instrum* 2009, 80, 054901. [PubMed: 19485524]
- (45). Yao D-K; Zhang C; Maslov K; Wang LV Photoacoustic Measurement of the Gruneisen Parameter of Tissue. *J. Biomed. Opt* 2014, 19, 017007.
- (46). Hariri A; Alipour K; Mantri Y; Schulze JP; Jokerst JV Deep Learning Improves Contrast in Low-Fluence Photoacoustic Imaging. *Biomed. Opt. Express* 2020, 11, 3360–3373. [PubMed: 32637260]
- (47). Xiang Y; Wu X; Liu D; Li Z; Chu W; Feng L; Zhang K; Zhou W; Xie S Gold Nanorod-Seeded Growth of Silver Nanostructures: From Homogeneous Coating to Anisotropic Coating. *Langmuir* 2008, 24, 3465–3470. [PubMed: 18294010]
- (48). Katz-Boon H; Walsh M; Dwyer C; Mulvaney P; Funston AM; Etheridge J Stability of Crystal Facets in Gold Nanorods. *Nano Lett.* 2015, 15, 1635–1641. [PubMed: 25658226]
- (49). Petrova E; Liopo A; Oraevsky AA; Ermilov SA Temperature-Dependent Optoacoustic Response and Transient through Zero Grüneisen Parameter in Optically Contrasted Media. *Photoacoustics* 2017, 7, 36–46. [PubMed: 28725558]
- (50). Xu S; Scherer GW; Mahadevan TS; Garofalini SH Thermal Expansion of Confined Water. *Langmuir* 2009, 25, 5076–5083. [PubMed: 19275191]
- (51). Hariri A; Lemaster J; Wang J; Jeevarathinam AS; Chao DL; Jokerst JV The Characterization of an Economic and Portable Led-Based Photoacoustic Imaging System to Facilitate Molecular Imaging. *Photoacoustics* 2018, 9, 10–20. [PubMed: 29234601]
- (52). Cavigli L; Khlebtsov BN; Centi S; Khlebtsov NG; Pini R; Ratto F Photostability of Contrast Agents for Photoacoustics: The Case of Gold Nanorods. *Nanomaterials* 2021, 11, 116.
- (53). Sadovnikov SI; Gusev AI Thermal Expansion, Heat Capacity and Phase Transformations in Nanocrystalline and Coarse-Crystalline Silver Sulfide at 290–970 K. *J. Therm. Anal. Calorim* 2018, 131, 1155–1164.
- (54). Sun L; Yan X; Zheng J; Yu H; Lu Z; Gao S.-p.; Liu L; Pan X; Wang D; Wang Z; Wang P; Jiao L Layer-Dependent Chemically Induced Phase Transition of Two-Dimensional Mos2. *Nano Lett.* 2018, 18, 3435–3440. [PubMed: 29782176]
- (55). Smith DK; Korgel BA The Importance of the Ctab Surfactant on the Colloidal Seed-Mediated Synthesis of Gold Nanorods. *Langmuir* 2008, 24, 644–649. [PubMed: 18184021]
- (56). He J; Unser S; Bruzas I; Cary R; Shi Z; Mehra R; Aron K; Sagle L The Facile Removal of Ctab from the Surface of Gold Nanorods. *Colloids Surf., B* 2018, 163, 140–145.
- (57). Cheah MH; Chernev P Electrochemical Oxidation of Ferricyanide. *Sci. Rep* 2021, 11, 23058. [PubMed: 34845249]
- (58). Loo BH; Lee YG; Liang EJ; Kiefer W Surface-Enhanced Raman Scattering from Ferrocyanide and Ferricyanide Ions Adsorbed on Silver and Copper Colloids. *Chem. Phys. Lett* 1998, 297, 83–89.

- (59). Sugiyama A; Miura M; Oshikiri Y; Kim Y; Morimoto R; Miura M; Osaka T; Mogi I; Yamauchi Y; Aogaki R Excess Heat Production in the Redox Couple Reaction of Ferricyanide and Ferrocyanide. *Sci. Rep* 2020, 10, 20072. [PubMed: 33208775]
- (60). Chang CC; Bocarsly AB Oxidation of Halides by Redox Enhanced Ferricyanide in the $[\text{Fe}^{\text{II}}\text{-CN-Pt}^{\text{IV}}]$ N Coordination Polymer: An Optically Triggered Process. *J. Electroanal. Chem* 1999, 470, 99–113.
- (61). Ramalingam K; Liang M; Pyae NLW; Aung SH; Oo TZ; Srimuk P; Ma J; Presser V; Chen F; Waite TD Self-Sustained Visible-Light-Driven Electrochemical Redox Desalination. *ACS Appl. Mater. Interfaces* 2020, 12, 32788–32796. [PubMed: 32597634]
- (62). Kay HF Electrostriction. *Rep. Prog. Phys* 1955, 18, 230–250.
- (63). Villafañe V; Sesin P; Soubelet P; Anguiano S; Bruchhausen AE; Rozas G; Carbonell CG; Lemaître A; Fainstein A Optoelectronic Forces with Quantum Wells for Cavity Optomechanics in Gaas/Alas Semiconductor Microcavities. *Phys. Rev. B* 2018, 97, 195306.
- (64). Wang X; Nie S; Li J; Clinite R; Wartenbe M; Martin M; Liang W; Cao J Electronic Grüneisen Parameter and Thermal Expansion in Ferromagnetic Transition Metal. *Appl. Phys. Lett* 2008, 92, 121918.
- (65). Knyazev G; Ignatyeva D; Sopko I; Belotelov V; Romanov O Amplification of the Electrostriction Mechanism of Photoacoustic Conversion in Layered Media. *J. Phys. D: Appl. Phys* 2020, 53, 475101.
- (66). Heritier J-M Electrostrictive Limit and Focusing Effects in Pulsed Photoacoustic Detection. *Opt. Commun* 1983, 44, 267–272.
- (67). Feitelson J; Mauzerall D Enthalpy and Electrostriction in the Electron-Transfer Reaction between Triplet Zinc Uroporphyrin and Ferricyanide. *J. Phys. Chem. B* 2002, 106, 9674–9678.
- (68). Autrey T; Foster NS; Klepzig K; Amonette JE; Daschbach JL A New Angle into Time-Resolved Photoacoustic Spectroscopy: A Layered Prism Cell Increases Experimental Flexibility. *Rev. Sci. Instrum* 1998, 69, 2246–2258.
- (69). Dziaugys A; Kelley K; Brehm JA; Tao L; Poretzky A; Feng T; O'Hara A; Neumayer S; Chyashnavichyus M; Eliseev EA Piezoelectric Domain Walls in Van Der Waals Antiferroelectric $\text{CuInP}_2\text{Se}_6$. *Nat. Commun* 2020, 11, 3623. [PubMed: 32681040]

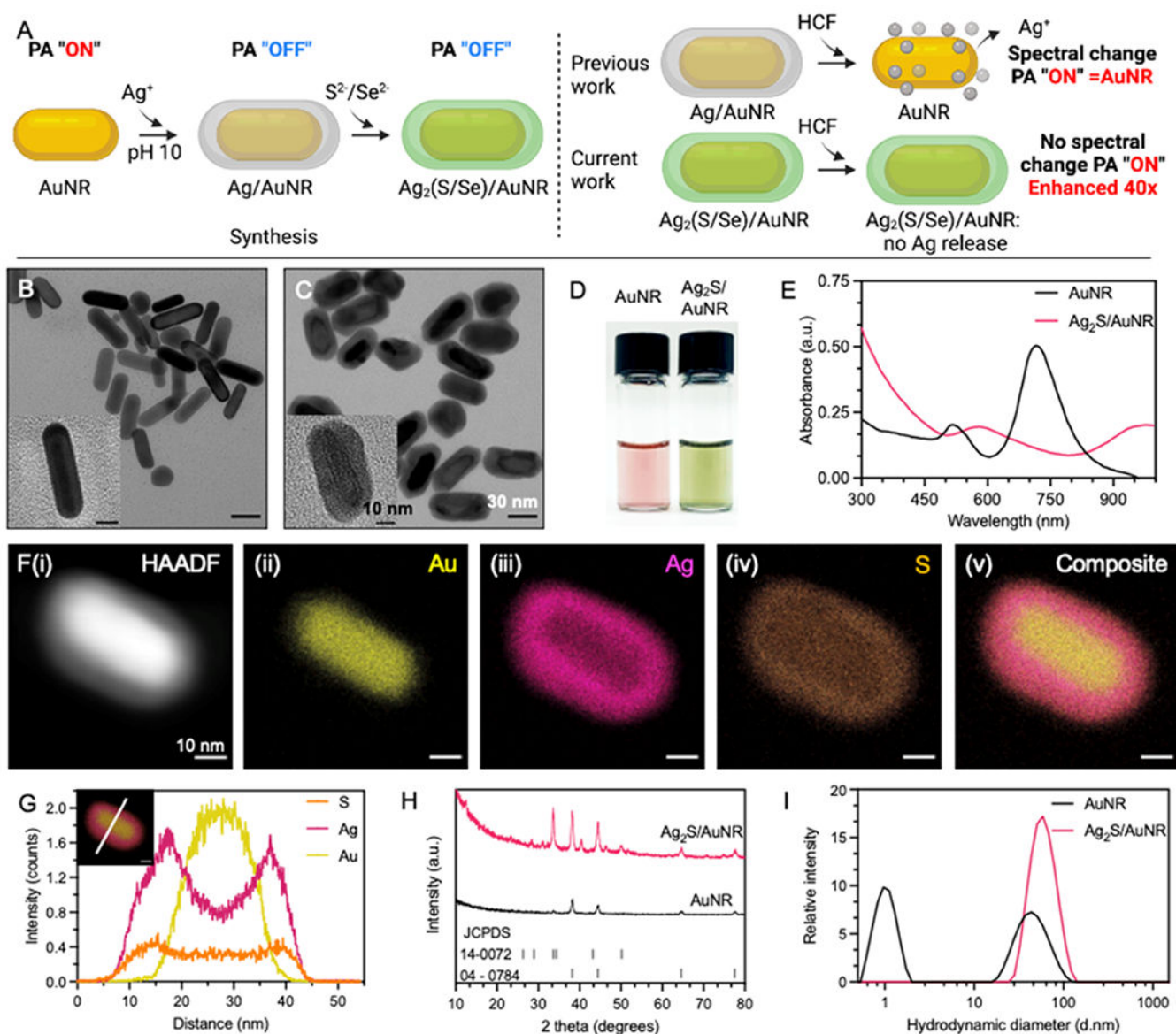


Figure 1.

Ag₂S/AuNR synthesis and characterization. (A) Schematic representation of silver chalcogenide-coated AuNR synthesis and HCF treatment. (B,C) TEM images of synthesized AuNRs and the Ag₂S/AuNR show a core-shell particle (insets: HR-TEM images). The AuNR aspect ratios were 3.08 ± 0.35 , and the Ag₂S shell thickness was 7.3 ± 1.4 nm. Scale bars on low- and high-resolution images are 30 and 10 nm, respectively. (D) Addition of a Ag₂S shell changes the AuNR suspension color from pale pink to green. (E) Synthesized AuNRs had a characteristic absorption spectrum peak at 710 nm. The Ag₂S shell coatings lead to a red shift and attenuation of the spectrum into the infrared region. (F,G) EDX mappings of the Ag₂S/AuNR confirm a gold nanorod core and a Ag₂S shell formation. Scale bars represent 10 nm. (H) pXRD analysis of the Ag₂S/AuNR shows characteristic crystal facets for both Ag₂S and Au. (I) DLS spectra show an 8.1 nm increase in the particle hydrodynamic diameter after the Ag₂S coating.

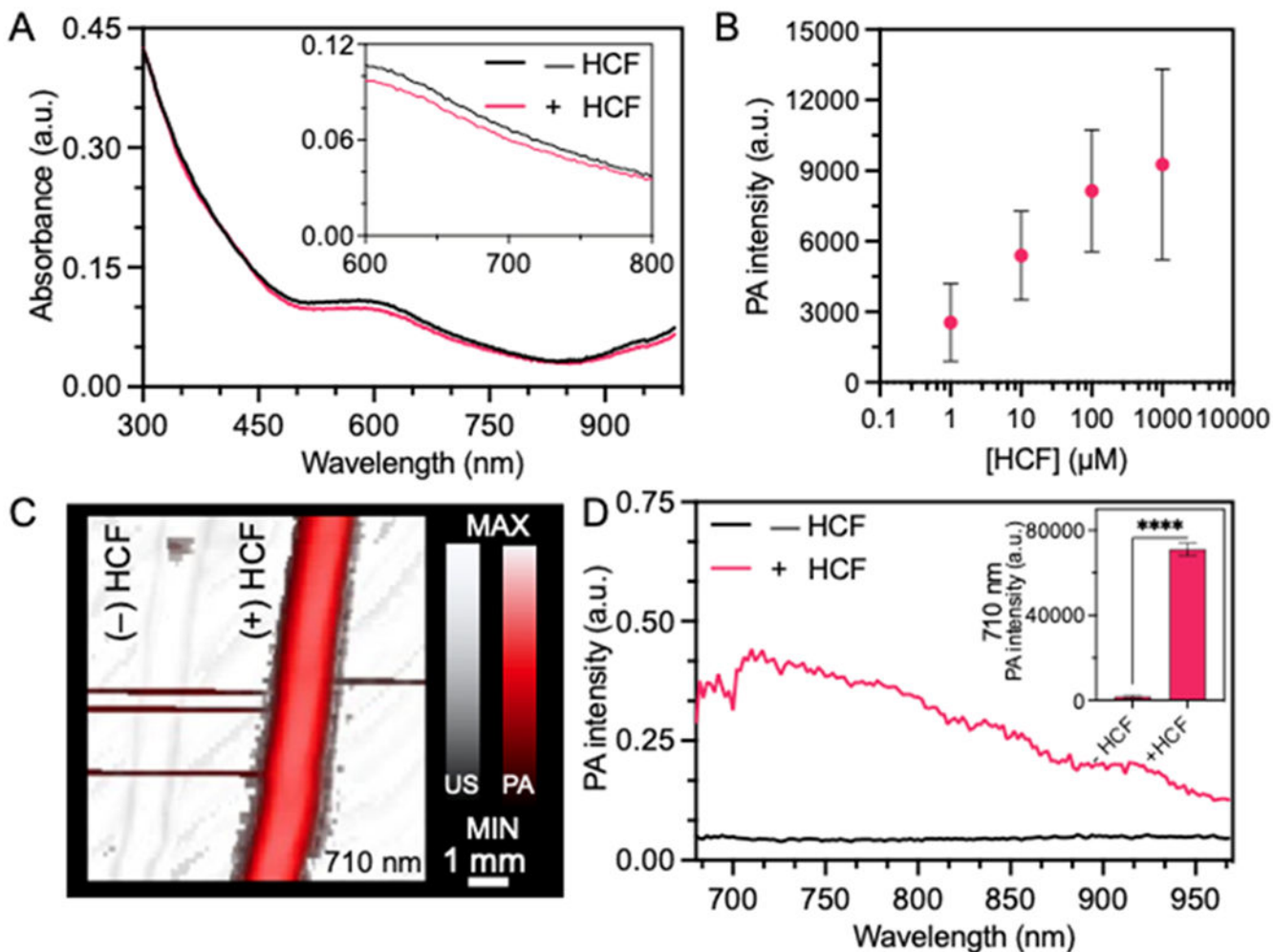


Figure 2.

HCF-mediated PA enhancement of $\text{Ag}_2\text{S}/\text{AuNR}$. There was no change in absorbance but a 42-fold PA enhancement. (A) HCF treatment of $\text{Ag}_2\text{S}/\text{AuNR}$ s causes no significant changes in the absorption spectrum. (B) $\text{Ag}_2\text{S}/\text{AuNR}$ s stabilized in 5 mM CTAB show an exponential PA enhancement with increasing amounts of HCF. (C,D) HCF-treated particles show a significant (42-fold) PA enhancement at 710 nm ($p < 0.0001$). (D) The PA spectrum of untreated particles follows the low absorbance pattern in (A). HCF-treated particles have a peak PA signal at 710 nm. 710 nm is the LSPR of the core gold nanorod. The error bars represent the standard deviation of six ROIs.

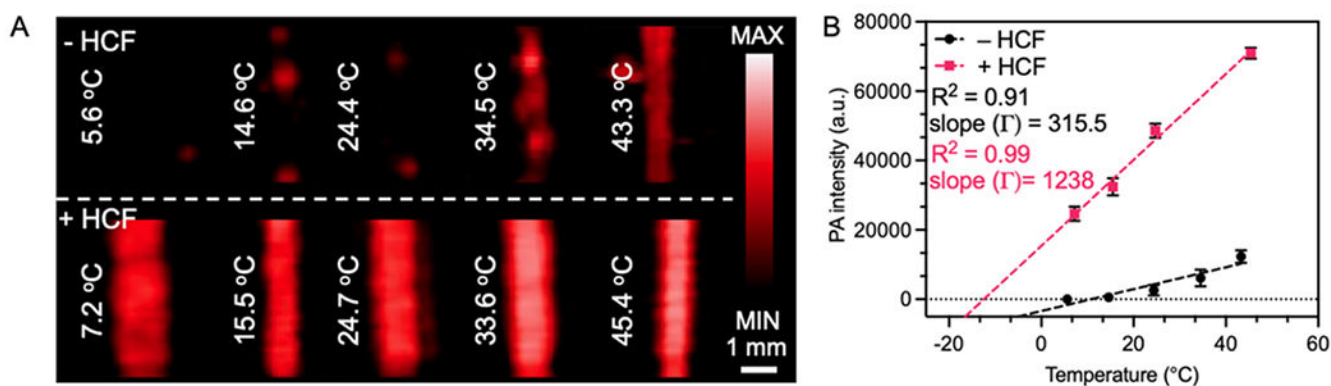


Figure 3. Change in the Grüneisen parameter (Γ) of the Ag₂S/AuNR after HCF treatment. (A,B) HCF-treated Ag₂S/AuNRs have nonzero PA intensity in the 0–4 °C range. This suggests that PA enhancement is independent of the solvent due to thermal confinement with the nanoparticle and its shell. The slope in (B) represents Γ . HCF-treated particles show a significant 4-fold enhancement in Γ ($p < 0.001$).

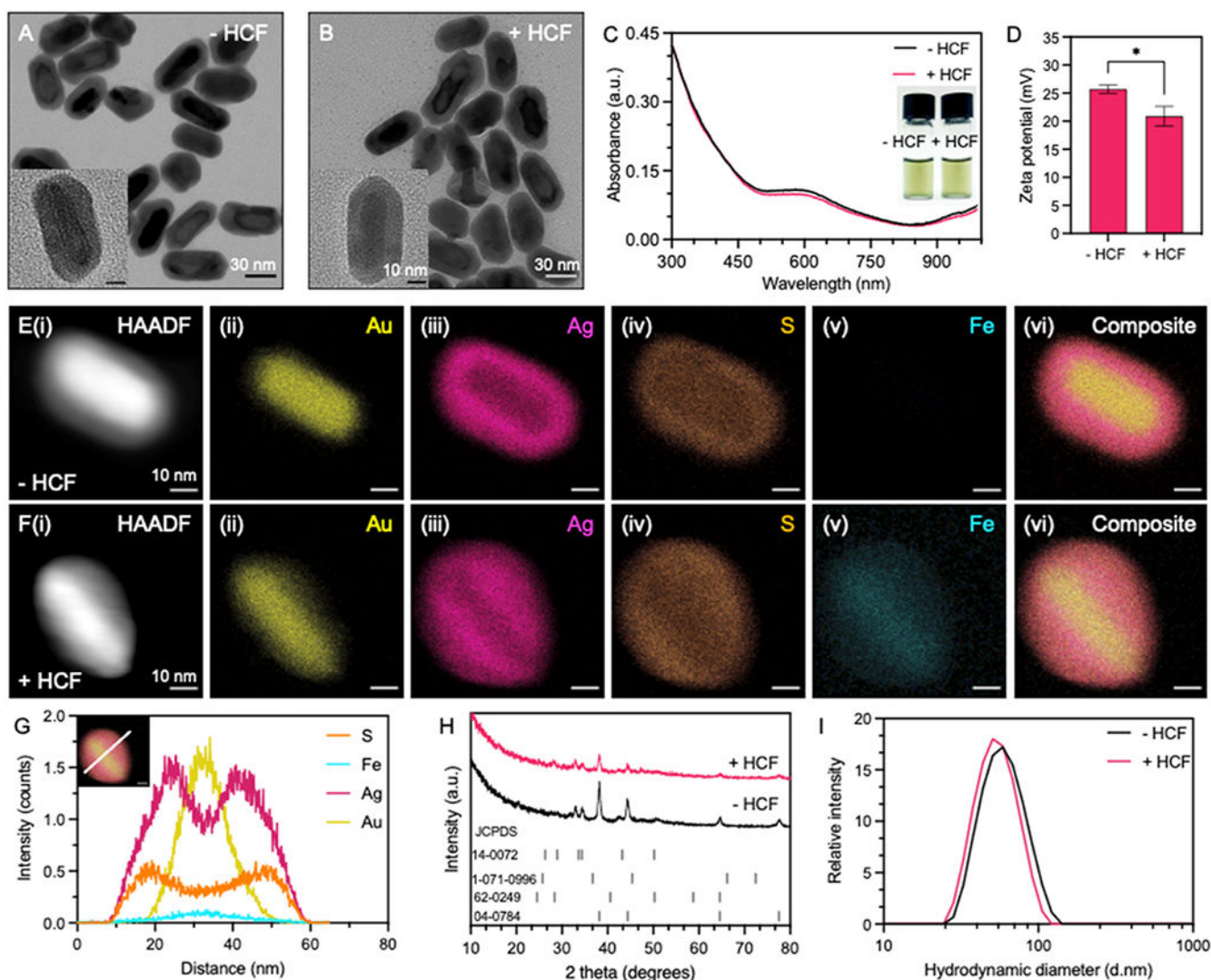


Figure 4.

Ag₂S/AuNR characterization after HCF treatment. (A,B) TEM images of Ag₂S/AuNR before and after HCF addition show conservation of the core–shell structure, particle size, shell thickness, and colloidal stability (insets: HR-TEM images). This contrasts with our previous work where the Ag shell was selectively oxidized using HCF.¹¹ Scale bars on low- and high-resolution images measure 30 and 10 nm, respectively. (C) Absorption spectra remain unchanged after HCF treatment. (D) There is a significant ($p < 0.05$) reduction in the zeta potential due to the adsorption of negatively charged HCF on positively charged and CTAB-stabilized particles. (E,F) EDX mappings of the Ag₂S/AuNR before and after HCF treatment show the surface adsorption of Fe representing [Fe(CN)₆]³⁻. (G) EDX mapping of the HCF-treated Ag₂S/AuNR shows slight favoring of Fe adsorption along the longitudinal edge of the particle which is also seen in [F(v)]. (H) pXRD spectra showed no change in the crystal structure upon HCF treatment. JCPDS cards 04-0784 (Au), 62-0249 (γ -Ag₂S), 1-071-0996 (β -Ag₂S), and 14-0072 (α -Ag₂S). (I) DLS spectra show no significant change

in the particle hydrodynamic diameter after HCF treatment ($p > 0.05$). Error bars in (D) represent standard deviation across six measurements.

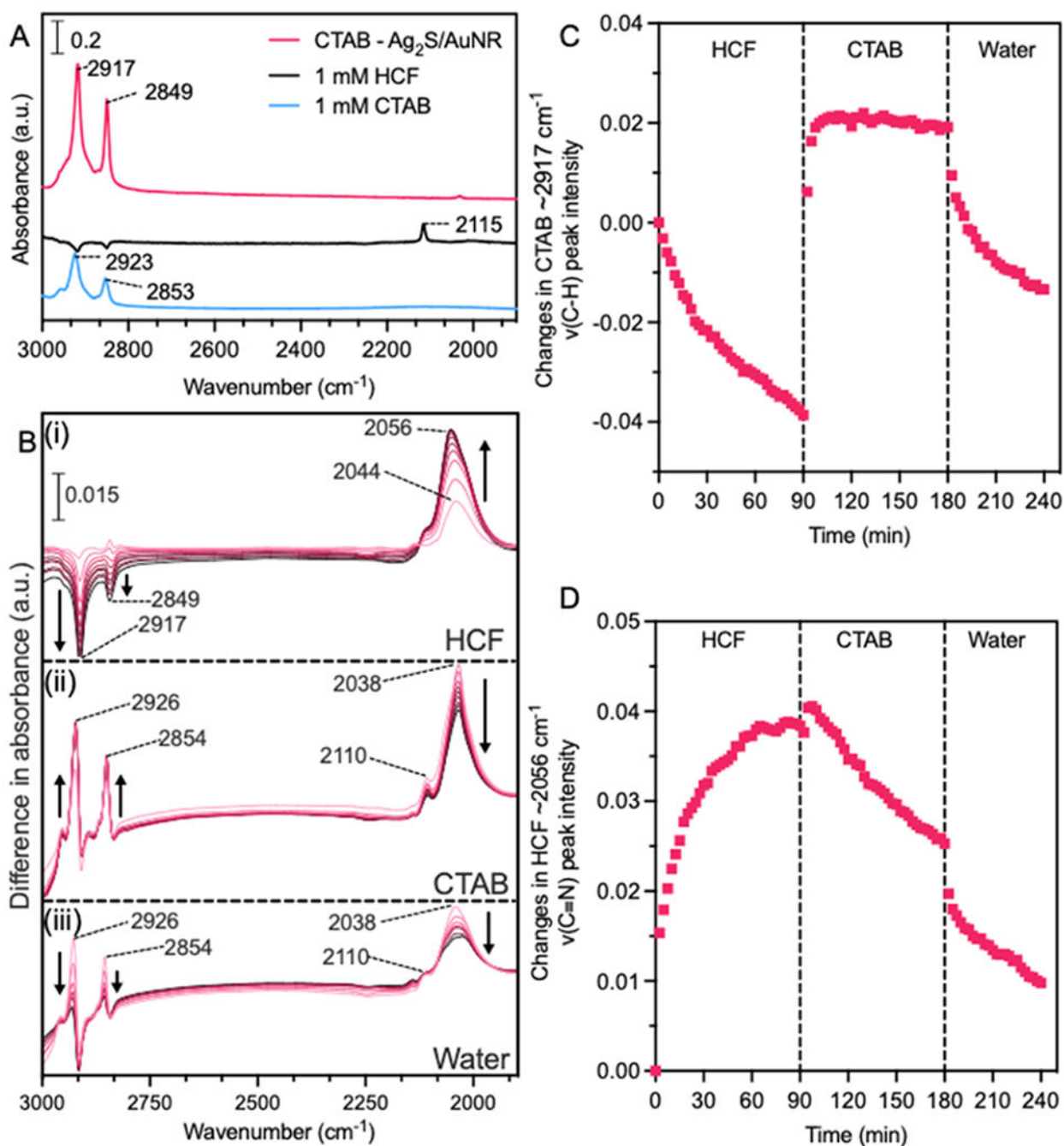


Figure 5.

Dynamic in situ ATR-FTIR spectra of the $\text{Ag}_2\text{S}/\text{AuNR}$ upon HCF treatment. (A) Reference spectra for a dried thin film of the CTAB-stabilized $\text{Ag}_2\text{S}/\text{AuNR}$ on an AMTIR crystal; 1 mM solution-phase HCF and 1 mM solution-phase CTAB are shown. (B) Here, in situ time-dependent ATR-FTIR difference spectra for a CTAB-stabilized $\text{Ag}_2\text{S}/\text{AuNR}$ following (i) $50 \mu\text{M}$ HCF flow adsorption. Increase in the 2056 cm^{-1} $\nu(\text{C}\equiv\text{N})$ band with the simultaneous decrease in the 2917 and 2849 cm^{-1} $\nu(\text{C}-\text{H})$ bands as a function of time suggests a displacement of CTAB with HCF. (ii) $50 \mu\text{M}$ CTAB flow adsorption following

HCF adsorption. CTAB can partially desorb loosely bound HCF while forming multilayers on direct surface-bound HCF as seen by a change in the peak intensity as a function of time. (iii) Water desorption flow. These spectra show the desorption of multilayer CTAB and changes to the surface coordination of adsorbed HCF. Temporal spectra in (B) are collected every 10 min from light to dark coloration. (C) Changes in the CTAB $\sim 2917\text{ cm}^{-1}$ $\nu(\text{C-H})$ peak intensity. (D) Changes in the HCF 2056 cm^{-1} $\nu(\text{C}\equiv\text{N})$ peak intensity.